Three-dimensional porous structure reconstruction based on structural local similarity via sparse representation on micro-computed-tomography images

Yuzhu Wang, Ji-Youn Arns, Sheikh S. Rahman, and Christoph H. Arns*
School of Minerals and Energy Resources Engineering, UNSW Australia, Sydney NSW 2052, Australia

(Received 27 May 2017; published 29 October 2018)

A tomographic or image representation of three-dimensional (3D) porous media is a primary tool for the consistent correlation and prediction of multiple physical properties. For multiscale media a single imaging scale may not be sufficient, and a compromise between field of view and resolution is required. The resulting lower resolution compared to relevant length scales in part of the tomogram impacts on the quality of petrophysical cross-correlations. This situation is overcome in geostatistics by carrying out stochastic simulations with lower resolution constraints and propagating uncertainty from smaller scales through upscaling procedures capturing the behavior of the system at smaller scales. Applying this technique to full tomograms requires a fast high-resolution reconstruction technique. We propose a local-similarity statistic reconstruction (LSSR) method to reconstruct 3D high-resolution porous structure by combining a set of increasing resolution micro-computed-tomography (micro-CT) images with decreasing field of view (FOV) to overcome this limitation. The reconstruction technique is based on two assumptions, universally existent local similarity at a given scale and fixed image degradation when downscaling by the same factor between corresponding cubes of high- and low-resolution images. Utilizing the flexibility of micro-CT images in terms of resolution and FOV, a sample was scanned first with low resolution, and then a subset was taken from this sample and scanned with high resolution. A significant number of small cube pairs are extracted from corresponding parts of the low-resolution and high-resolution images, where both high- and low-resolution images are accessible. These cube pairs contain abundant information about features of local porous structure under different resolutions allowing reconstruction of a higher-resolution micro-CT image. Instead of the "Search-Statistic" strategy popularly used in current reconstruction algorithm a "Decomposition-Reconstruction" strategy is applied to accelerate computations and improve the reconstruction accuracy. Local porosity theory and the Minkowski measures are used to estimate the performance of reconstruction algorithms. Compared to multipoint statistics we improve computational efficiency by employing a sparse representation and principal component analysis for compression, while also improving on reconstruction accuracy.

DOI: 10.1103/PhysRevE.98.043310

I. INTRODUCTION

A three-dimensional (3D) representation of disordered porous media is frequently used to predict transport properties and derive consistent cross-correlations of physical properties. This is particularly the case for materials with strong property contrasts, e.g., at the pore scale, and where heterogeneity exists at multiple scales. For this class of materials bounds on effective physical properties may be less tight (e.g., the lower Hashin-Shtrikman bounds [1] may be zero). The complexity of multiscale heterogeneous materials makes it difficult to choose effective medium theories with implicit microstructure representing their physical properties for consistent cross-correlations ([2,3]) while higher-order correlation functions as used in the Milton bounds [4] to constrain effective physical property predictions would be difficult to apply. Consequently, imaging methods have been used [5] with constantly improving field of view (FOV) and resolution. The latter are two opposing targets where a compromise needs to be made: large FOV allows the effective characterization of larger-scale heterogeneity, yet to the detriment of resolution necessary to calculate transport properties accurately. A potential solution to this problem are stochastic methods which honor low-resolution imaging data offering a large field of view, while capturing small-scale structural variability as basis for the calculation of consistent cross-correlations. In the following we recapture some of the common reconstruction techniques before setting out the organization of this article in detail. We target the development of a fast reconstruction technique for integrating small-scale variability into micro-computed-tomography (micro-CT) images by applying subresolution stochastic modeling.

A. Common stochastic reconstruction methods

There are two common ways to derive the 3D structure of a porous material: statistical reconstruction and direct imaging. Before the widespread use of micro-CT and focused ion beam ablation combined with scanning electron miscroscopy numerical reconstruction used to be the main approach to 3D porous structure modeling. Statistical reconstruction remains popular because of relative cost advantages and convenience and by extending the application of 3D imaging methods

*c.arns@unsw.edu.au

like micro-CT. For a long time since Fatt carried out flow simulations in a regular two-dimensional (2D) network model [6] porous media reconstruction and flow simulation were restricted to the 2D case because of computational limitations. Quiblier [7] proposed a 3D porous structure reconstruction method based on the measurements of characteristics using 2D thin sections of porous media. This method is based on successively passing a normalized uncorrelated Gaussian random field through a linear and then a nonlinear filter to generate the discrete values representing the phases of the structure [8]. This method is quite general [9] and robust [10], which attracted a large number of researchers to apply and develop it further in the subsequent two decades [8,11–14]. Kikkinides [15–17] proposed a porous structure reconstruction method based on fractional Brownian motion (fBm) models which has been successfully applied in porous media such as sandstone and membranes. The method is based on the midpoint displacement and successive random addition technique, which is, essentially, a graphical reproduction technique for the generation of self-affine media that follow fBm statistics. Using one- and two-point probability functions to reproduce more complex porous structures [8] may not reproduce connectivity properties critical for transport [18]. Morphological descriptors containing connectivity information were introduced as additional constrains into the reconstruction process, e.g., a two-point cluster function, lineal-path length, and chord-length function [8,13,19,20]. Since it is difficult to incorporate these new descriptors into the aforementioned filtering method, a simulated annealing (SA) method was proposed to reconstruct images subject to various statistical constrains [8,21,22]. Although reconstructions of several materials including sandstone [23] and chalk [24] were successful, the resulting images do not always capture the long-range connectivity of pore space, namely, for low porosity and particular media [25]. Another recent approach is process-based reconstruction, which mimics the geological process of the forming of sedimentary rocks [26–35]. A necessary precondition for use of this method is an adequate understanding of the physical and chemical processes essential to the formation of the porous structure and which is always difficult, especially in carbonates and shale.

A Markov chain Monte Carlo (MCMC) reconstruction method was developed by Wu *et al.* [36] to simulate 2D soil images effectively. This algorithm was extended to 3D porous structure modeling in their subsequent work through using three perpendicular 2D sections. These three sections are used as prior in determining the transition probabilities controlling the Markov chain process. The MCMC method was further generalized to multipoint statistics (MPS) by Okabe and Blunt [9,37], which was introduced in geostatistics to represent connected geobodies at field scale by Strebelle *et al.* [38]. Since then, the reconstruction of 3D images is based mainly on 2D images. With the increasing availability of micro-CT images of porous structures, a tomography-associated MPS method has been developed [39] as well as grain-based reconstruction methods including tomographic information [40]. In these methods macropores are identified by micro-CT, while micropores are provided by MPS or grain reconstruction and then superimposed to obtain the final image with an improved connectivity. Another recent approach introduces a reconstruction method utilizing low-resolution information and a subpixel model, where the latter correlates subresolution pore size to the porosity of voxels, which are not completely void [41].

B. Computational cost of MPS

The accuracy of the MPS method depends on the size of the scanning template and the number of replica that can be searched in the training image. Larger template sizes are computationally much more demanding and also imply a reduced number of replicas available for training. Comunian *et al.* [42] summarize time requirements for the MPS method against template size and show that using a 3D template with a size of $7 \times 7 \times 7$ voxel will consume more than two orders of magnitude greater computing time than required by using a 2D template. Thus, the main problem is balancing template size and number of replicas.

C. Work flow and organization of this article

To overcome the contradiction between resolution and FOV, we propose a mathematical method called local-similarity-based statistical reconstruction (LSSR) to reconstruct a high-resolution micro-CT image. We use a sparse presentation algorithm to determine (train) a dictionary by which to reconstruct the expected high-resolution cubes. A decomposition step is introduced that projects the low-resolution cube onto a trained low-resolution dictionary and derives its projection coefficients (namely, sparse coefficients). Reconstruction is then a linear combination of high-resolution dictionary entries based on these projection coefficients. Because of local-similarity features (defined in detail in Sec. II), identical sparse coefficients are used in low- and high-resolution dictionary training. Figure 1 illustrates the six steps in the work flow of the LSSR algorithm. Step 1 and step 2 are carried out interactively.

First. a tomogram of a relatively large sample (e.g., 25.4 mm diameter and 38 mm length) is acquired by micro-CT with a relatively low resolution (e.g., 16 μm). Then a cylindrical subplug is extracted from this large sample and scanned by micro-CT with a relatively high resolution (e.g., 4 μm). This process guarantees that there exists an overlap area where both high- and low-resolution images are accessible. In step 3, both the large FOV low-resolution image and the smaller FOV high-resolution subset are segmented into a limited number of discrete phases. In step 4, a large number of high- and low-resolution image cube pairs are extracted from the overlap area, and these image cubes record the structural characteristics of local structure under different resolution. In step 5, the high- and low-resolution dictionaries are trained via a sparse representation algorithm based on these image cube pairs. These two dictionaries can be treated as prior for the subsequent reconstruction work, and the calculation of these two dictionaries is the core of the LSSR method, which will be described in detail in the following sections. In step 6, the high-resolution estimation of any low-resolution cube outside the overlap area can be reconstructed based on the low- and high-resolution dictionaries obtained before. This process is

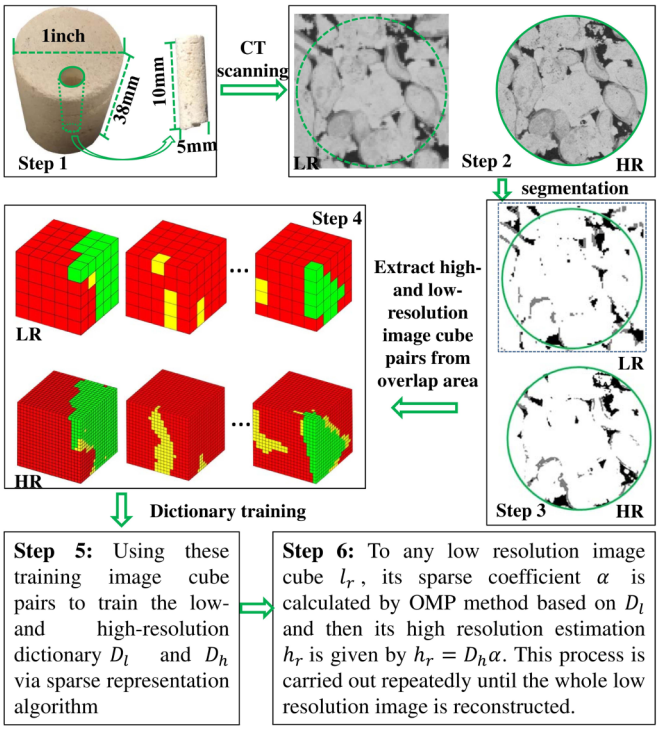

FIG. 1. Schematic work flow of the proposed LSSR technique. Note that the whole 2.54 cm diameter sample is scanned at relatively low resolution, while the subset can be scanned at higher resolution. LR and HR stand for low- and high-resolution image, respectively; OMP stands for orthogonal matching pursuit algorithm.

carried out repeatedly until the whole low-resolution image is reconstructed at high resolution.

The remainder of this work is organized as follows. In the next section, two 100^3 voxel pore-scale structure samples, extracted from Fontainebleau sandstone and Indiana limestone, will be used as examples to illustrate the features of local similarity. We then describe the work flow of the local-similarity-based statistical reconstruction (LSSR) in detail including a pseudocode of LSSR. This is followed by two cases of LSSR high-resolution porous structure reconstruction based on the Fontainebleau sandstone and Indiana limestone samples. The performance of LSSR is compared with the MPS approach using local porosity and theory and percolation probabilities [43,44] as well as Minkowski functionals [45–48].

II. STRUCTURAL LOCAL SIMILARITY

The proposed reconstruction technique is based on two assumptions, universally existing local similarity of the porous structure and a fixed image-degradation mechanism. We take local similarity of a rock sample to mean that for any chosen small test volume from the sample there is a very high probability that similar volumes (also called "neighbors" [49,50]) in terms of structure and component types (varies kinds of phases) also exist in the sample at other locations and thus can be searched. Considering a small volume, the number of its neighbors depends on the size of the test volume, number of phases and complexity of structure. Fixed image-degradation mechanism guarantees that if a sample is scanned two times

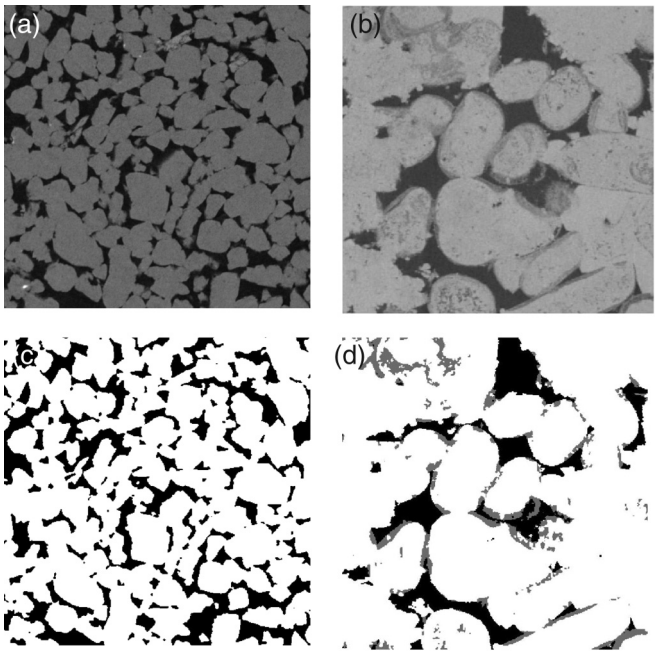

FIG. 2. Slices through the tomographic images of (a) Fontainebleau sandstone (600^3, $\epsilon = 2.9\,\mu$m) and (b) Indiana limestone (400^3, $\epsilon = 4\,\mu$m). (c) and (d) Segmented images corresponding to panels (a) and (b).

with different resolution, two small volumes extracted from the high-resolution image are similar when their corresponding low-resolution partners are similar.

The extracted cubes (template size in MPS literature) are relatively small (e.g., $5 \times 5 \times 5$ voxel) and typically contain a local structural feature, for example, a piece of a pore boundary. That, and the fact that we are working with segmented images containing a small number of phases, ensures that we can always find similar cubes within a porous structure. We choose the Hamming distance d_{st} as similarity measurement [51,52]

$$d_{st} = [\#(x_{ijk} \neq y_{ijk})/n], \tag{1}$$

where x_{ijk} and y_{ijk} are elements located at voxel ijk of data sets X and Y, respectively, and i, j, k denote (Cartesian) grid indices. $\#(x_{ijk} \neq y_{ijk})$ is the number of nonidentical elements between X and Y, and n is the number of elements in X or Y. The Hamming distance thus measures the fraction of nonidentical elements between two data sets; a Hamming distance of 0 shows the two data sets to be identical, and for a Hamming distance of 0.1 10% of the elements of the two data sets are different.

A. Samples

The Fontainebleau sandstone and Indiana limestone samples used in this study are shown in Fig. 2. The tomogram of Fontainebleau sandstone has an isotropic resolution of $\epsilon = 2.9\,\mu$m with a size of 600^3 voxel, where a voxel is a cubic element of size ϵ^3 [Fig. 2(a)]. The tomogram of the Indiana limestone sample has a resolution of $\epsilon = 4.05\,\mu$m with a size of 400^3 voxel [Fig. 2(b)]. These two tomograms

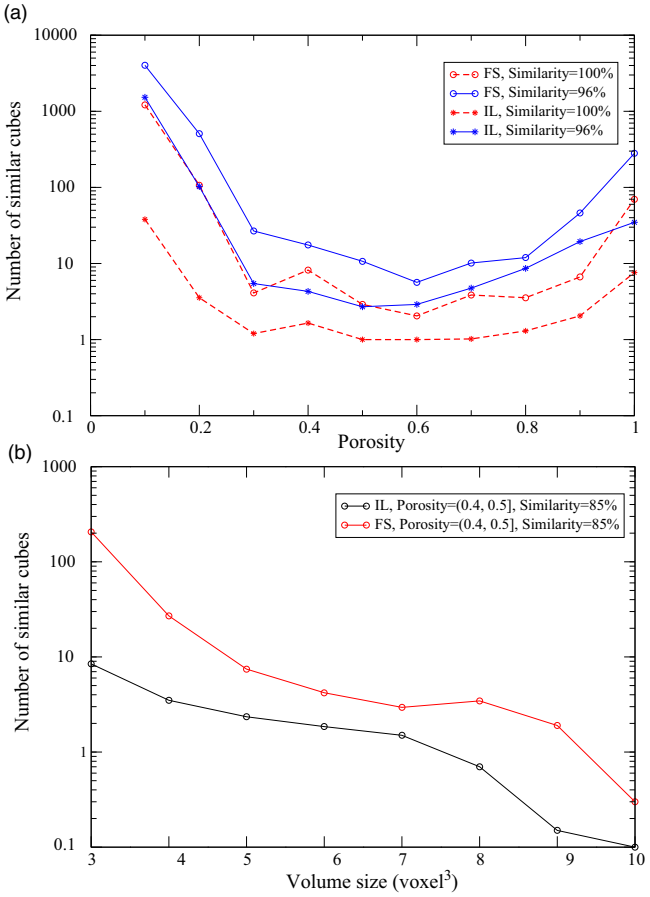

FIG. 3. Local-similarity analysis for Fontainebleau sandstone (FS) and Indiana limestone (IL). (a) Number of similar cubes change over porosity, volume size is $3 \times 3 \times 3$ voxels. (b) Number of similar cubes change over volume size.

are segmented by a converging active contour (watershed) algorithm using the MANGO software [53]. Compared to Fontainebleau sandstone, which is segmented into void and solid, Indiana limestone has an extra intermediate phase [Figs. 2(b) and 2(d)], which represents subresolution porosity typical for oolitic limestone and is determined by iterative application of the watershed algorithm.

B. Local similarity

Figure 3 depicts the probability to capture similar cubes for Fontainebleau sandstone and Indiana limestone. The difference between Fontainebleau sandstone and Indiana limestone is twofold: structural complexity and number of phases. We use Fontainebleau sandstone as example to illustrate the procedure of local-similarity analysis; Indiana limestone is processed in the same way. A 100^3 subset, S_f, is cropped from the Fontainebleau sandstone sample to analyze local similarity. Because the number of similar cubes also depends on the complexity of structure, porosity is considered when we count the number of similar cubes. The porosity varies from 0 to 1. This range is divided equally into 10 intervals (P_i, $i = 1, 2, \ldots, 10$, where P_1 denotes the porosity interval 0 to 0.1). For each porosity interval P_i, 20 edges containing cubes (C_i, $i = 1, 2, \ldots, 20$) with size of $L \times L \times L$ voxel are selected randomly from S_f. Edge-containing cubes are cubes containing more than one phase. For every cube C_i its similar cubes are then searched by scanning S_f. The average number of similar cubes of these 20 cubes is calculated as the similar cube numbers for P_i. As a structure parameter, porosity roughly reflects the complexity of the structure: the two ends of the porosity range represent simpler structure, and it is clear that the number of similar cubes at the two ends of the porosity range are much larger than for the intermediate porosity intervals [see Fig. 3(a)]. In addition, it is also clear that the number of similar cubes decreases rapidly along with the increase of template size [Fig. 3(b)]. Both Figs. 3(a) and 3(b) show that increasing the number of phases results in rapidly decreasing the count of similar cubes.

C. Fixed image degradation

Figure 4 illustrates the fixed image-degradation mechanism for Fontainebleau sandstone and Indiana limestone. Fixed image-degradation mechanism analyzes how similar two high-resolution image cubes are when their low-resolution partners are similar to each other. The similarity distribution depends on four aspects: structural complexity which is roughly represented by porosity (P), magnification factor (S), similarity in low-resolution image cubes (S_{im}), and cube size (C_s). Thus, the similarity distribution can be treated as a function of four parameters: P, S, S_{im}, and C_s. Here we use Indiana limestone as an example to introduce our procedure of analyzing fixed image-degradation mechanism. A $400 \times 400 \times 400$ voxel Indiana limestone sample image, HR_8 is extracted as test sample. This HR_8 image is down-sampled to three low-resolution images with sizes of 200^3, 100^3, and 50^3 voxel, denoted by HR_4, HR_2, and LR, respectively. Then any three parameters of (P, S, S_{im}, and C_s) are kept constant, and the fourth one is adjusted to analyze the change of the similarity distribution.

For example, in Fig. 4(a) the parameters $S = 4$, $S_{im} = 100\%$ and $C_s = 3$ are kept constant, and P is adjusted to analyze the relationship between porosity and similarity distribution. First, a 3^3 voxel cube ($C_s = 3$) with porosity of P [$P \in (0, 0.1)$], C_l, is randomly chosen from LR, and then a set of m similar cubes, denoted by C_{l1}, C_{l2}, C_{l3}, …, C_{lm}, searched on the low-resolution image, LR under similarity 100% ($S_{im} = 100\%$). Their m high-resolution partners, denoted by C_{h1}, C_{h2}, C_{h3}, …, C_{hm}, can be located in HR_4. The low-resolution test cube, C_l, also has its high-resolution partner, C_h. We quantify the similarity between C_h and C_{h1}, C_{h2}, C_{h3}, …, C_{hm} via computing their Hamming distance. The result is recorded in a $1 \times m$ vector, D. Second, considering the generality, 20 rather than one low-resolution cubes with $S = 4$ (identical to the former example), $P \in (0, 0.1)$, $C_s = 3$ and $S_{im} = 100\%$ are selected randomly and the first step repeated to obtain their Hamming distance vectors. The distribution of these Hamming distance vectors illustrates the similarity under the situation of $S = 4$, $P \in (0, 0.1)$, $C_s = 3$ and $S_{im} = 100\%$. Third, the first and second steps are repeated for different porosity values to obtain the respective similarity distribution features. The relationship between porosity and similarity distribution of Indiana limestone is presented in

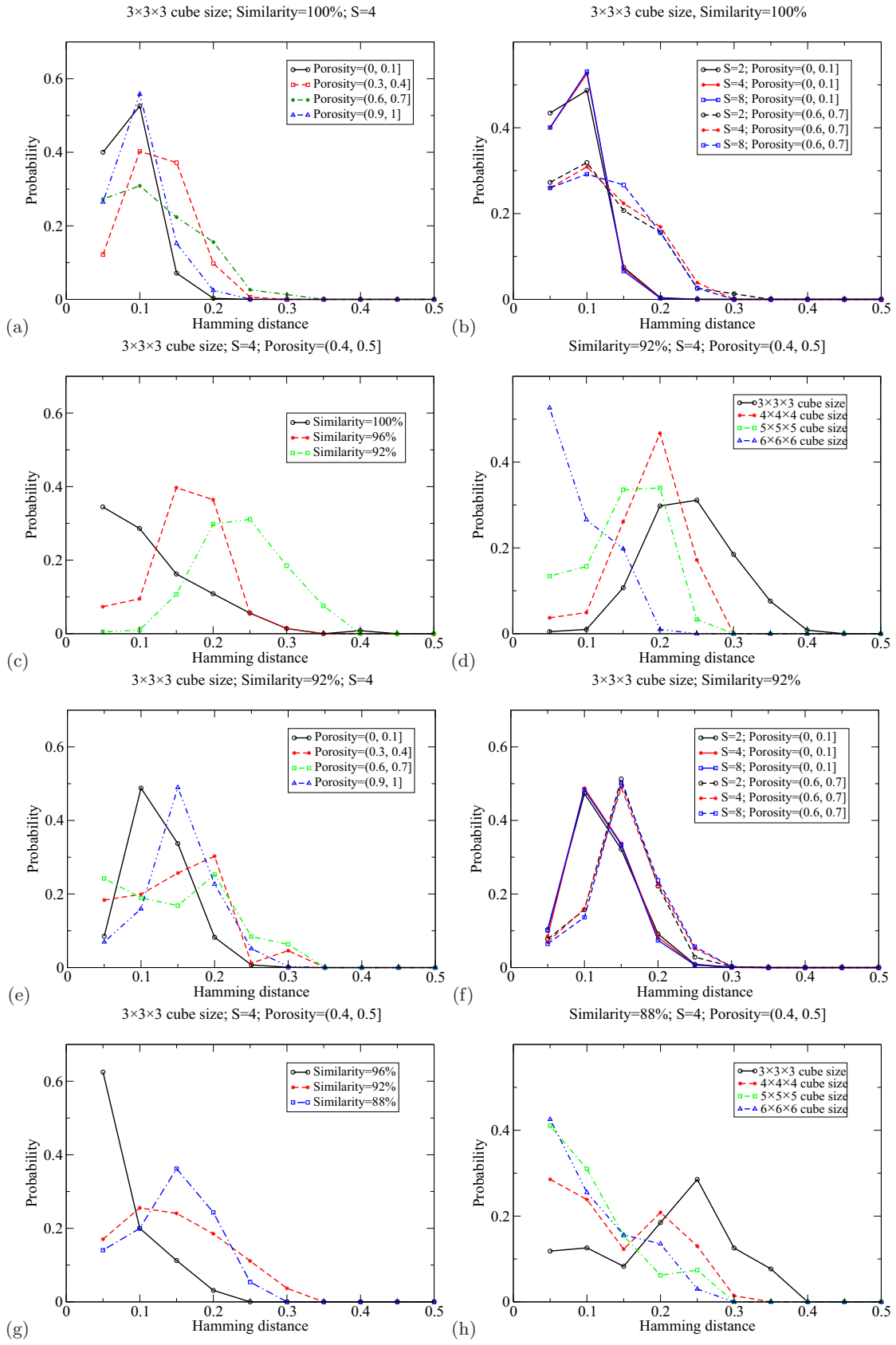

FIG. 4. Fixed image-degradation mechanism for Fontainebleau sandstone and Indiana limestone. (a)–(d) The distribution of the Hamming distance vector of Fontainebleau sandstone over porosity, magnification factor, and similarity in low-resolution image cubes and cubic size, respectively; (e)–(h) the distribution of the distance vector of Indiana limestone over porosity, magnification factor, and similarity in low-resolution image cubes and cubic size, respectively.

Fig. 4(e). Taking the red curve in Fig. 4(a) as an example, we see that if two $3 \times 3 \times 3$ voxel low-resolution cubes with porosity range from 0 to 0.1 are identical ($S_{im} = 100\%$) with each other, their $4\times$ high-resolution partners have about 40% probability to also be similar with each other with a similarity larger than 95%, and about 53% probability with a 90% to 95% similarity (Hamming distance 0.1 implies 90% similarity). Figures 4(a)–4(d) present the distribution of distance vectors of Fontainebleau sandstone over porosity (P), magnification factor (S), similarity in low-resolution image cubes (S_{im}), and cubic size (C_s), respectively. Figures 4(e)–4(h) presents the distribution of distance vector of Indiana limestone over porosity (P), magnification factor (S), similarity in low-resolution image cubes (S_{im}), and cubic size (C_s), respectively. From Fig. 4 it is clear that the reliability of fixed image-degradation mechanism is decreased along with the increase of structure complexity, but increased along with the decrease of similarity. The magnification factor has only a slightly effect on the similarity distribution. Although increasing cube size will result in a small number of similar cubes, the similarity distribution also will increase.

III. LOCAL-SIMILARITY-BASED STATISTIC RECONSTRUCTION

In general, all trainable image-processing algorithms consist of two steps, extracting statistical properties from training image(s) and using that information to process target images [54]. For example, the Gaussian random field reconstruction method (GRF) extracts a two-point correlation function from the training image as statistical property, and then calculates a linear filter based on the extracted two-point correlation function. Finally, the reconstructed image is obtained via convolving the linear filter with an initial image generated randomly to comply with a standard Gaussian distribution. Different from GRF, the statistical properties extracted from a training image in LSSR are a set of high and low-resolution image cube pairs and these image cube pairs are used to train a pair of high- and low-resolution dictionaries rather than a lineal filter. In GRF, the final reconstructed image is calculated by convolution. In LSSR the reconstructed image is obtained by a "Decomposition-Reconstruction" strategy discussed in the following sections.

A. Extract training image cube pairs

In this step, a set of high- and low-resolution cube pairs are extracted from the high- and low-resolution micro-CT image. High- and low-resolution images are noted by I_{high} and I_{low}, respectively. This allows us to derive a low-resolution image from a given one and then use this relationship to constraint the reconstruction of a higher-resolution image. We extract a large number (e.g., 30 000) of low-resolution cubes with a size of $c_l \times c_l \times c_l$ voxel from the low-resolution micro-CT image and their corresponding higher resolution patches with a size of $c_h \times c_h \times c_h$ voxel ($c_h = sc_l$) from the high-resolution segmented micro-CT image (see Fig. 5). These high- and low-image cubes are vectorized to column vectors with a dimension of c_h^3 and c_l^3, respectively. C_l and C_h are sets of these low- and high-resolution cube pairs whose elements are noted by l_r and h_r, respectively.

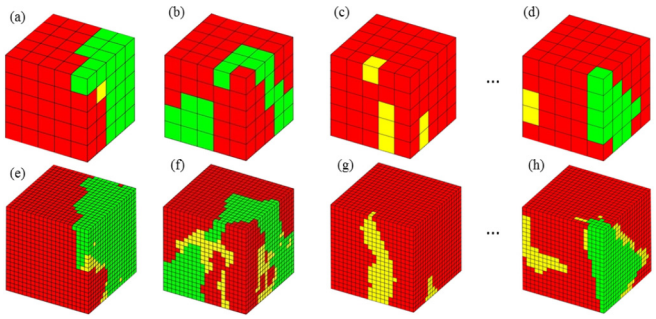

FIG. 5. Low- and high-resolution training image cubes pairs extracted from $16 \times 16 \times 16$ μm/voxel^3 resolution and $4 \times 4 \times 4$ μm/voxel^3 resolution Indiana limestone. (a)–(d) Low-resolution cubes with a size of $5 \times 5 \times 5$ voxel^3 and (e)–(h) corresponding high-resolution cubes with a size of $20 \times 20 \times 20$ voxel^3. The green, yellow, and red represent macropore and micropore clusters and a solid, respectively. These cube pairs record the structure relationship between low- and high-resolution images.

B. Dimensionality reduction

In the previous step all low- and high-resolution training image cube pairs have been organized into matrices C_l and C_h. The dimensionality of l_r and h_r is always extremely high. For example, if a template of $10 \times 10 \times 10$ voxel is used to scan the low-resolution cube and the magnification factor is 4, the dimensionality of l_r and h_r will be 1×1000 and $1 \times 64\,000$, respectively. If $n = 30\,000$ training image cube pairs are extracted, the dimensionality of C_h will be as high as $64\,000 \times 30\,000$, which results in heavy computation for following operations. We use principal component analysis (PCA) to reduce the dimension of the high-resolution training image cube vectors, but preserve most partial (e.g., 95%) average energy. Dimensionality reduction can improve the efficiency of algorithms greatly without obvious impact on reconstruction quality [55]. Assume that the size of C_h is $m \times n$ with $m = c_h^3$ for brevity. Every column of C_h represents a high-resolution cube, n is the number of high-resolution training cubes. The PCA operation for C_h is given by

$$\widetilde{C_h} = K C_h, \tag{2}$$

where C_h is the high-resolution training image cube matrix, $\widetilde{C_h}$ is the dimensionality reduced high-resolution training image cube matrix of dimension $m' \times n$, $m' \leqslant m$. K is the PCA transform matrix given by

$$\begin{aligned} K C_x K^* &= \Sigma \quad \text{with} \\ \Sigma &= \operatorname{diag}\left(\sigma_1^2, \sigma_2^2, \sigma_3^2, \ldots, \sigma_m^2\right), \\ \sigma_1^2 &\geqslant \sigma_2^2 \geqslant \sigma_3^2 \geqslant \cdots \geqslant \cdots \sigma_m^2. \end{aligned} \tag{3}$$

Here C_x is the covariance matrix of C_h, which is a symmetric positive semidefinite matrix. K^* is the conjugate transpose of K, which is a unitary matrix. Σ is a diagonal matrix consisting of the eigenvalues of C_x, and K is the corresponding eigenfaces matrix. Then the parameter m' can be determined

according to

$$\frac{\sum_{i=1}^{m'} \sigma_i^2}{\sum_{i=1}^{m} \sigma_i^2} = T. \tag{4}$$

T is a threshold which determines the ratio of energy we want to keep, and the first m' components are the best to keep in terms of minimizing the mean squared error from the original coefficient vector.

C. Dictionary learning

The low-resolution dictionary learning process is described by [50]

$$(D_l, \{\alpha_k\}) = \min_{D_l, \{\alpha_k\}} \sum_k \left(\| D_l \alpha_k - l_r^k \|^2 \right), \quad s.t. \parallel \alpha_k \parallel^0 \leqslant L. \tag{5}$$

Here D_l is the low-resolution dictionary, $\{\alpha_k\}$ is the set of sparse coefficients, and α_k denotes the sparse coefficient of the kth low-resolution cube; l_r^k denotes the kth low-resolution cube (the kth column of C_l). L is a small positive integer that determines the number of nonzero elements in α_k. The dictionary learning process consists of two steps, sparse coding and dictionary updating. We apply orthogonal matching pursuit (OMP) and K-SVD algorithms to solve these two steps, respectively. A pseudocode is given in the Appendix. For more details of the K-SVD algorithm and OMP we refer the reader to Aharon *et al.* [56] and Pati *et al.* [57]. The high-resolution dictionary, D_h, is then given by

$$D_h = \widetilde{C_h} A^\dagger = \widetilde{C_h} A^T (A A^T)^{-1}, \tag{6}$$

where $\widetilde{C_h}$ is the dimensionality-reduced set of high-resolution training cubes obtained from Eq. (2). A contains α_k as its columns and $A^\dagger$ is the pseudo-inverse of A.

D. Decomposition and reconstruction

Following the completion of the dictionary training step, we apply a 3D window with size $c_l \times c_l \times c_l$ voxel to raster scan the target low-resolution image, and a set of low-resolution cubes are extracted to generate a low-resolution cube matrix, denoted by L_m. l_m^k now denotes the k_{th} column of L_m, which represents a low-resolution cube of an image to reconstruct. Then the OMP method is used to obtain the sparse coefficients for the low-resolution cubes according to

$$\{\alpha_k'\} = \min_{\{\alpha_k'\}} \sum_k \left(\| D_l \alpha_k' - l_r^k \|^2 \right), \quad s.t. \parallel \alpha_k' \parallel^0 \leqslant L. \tag{7}$$

Here α_k' is the sparse coefficient of the low-resolution cubes of the image to reconstruct at high resolution, and D_l is the low-resolution dictionary from the previous training step [Eq. (5)]. L is a small positive integer that determines the number of nonzero elements in α_k'. Then the high-resolution cubes are reconstructed by

$$\widetilde{H_m} = D_h A', \tag{8}$$

where D_h is the high-resolution dictionary, A' contains $\{\alpha_k'\}$ as its columns, and $\widetilde{H_m}$ are the reconstructed high-resolution cubes. Notice that PCA is used to reduce the dimensionality of high-resolution training cubes, so the final high-resolution cubes are obtained by

$$H_m = K^{-1} \widetilde{H_m}, \tag{9}$$

where H_m are the final high-resolution cubes and K^{-1} is the inverse of the PCA transform matrix K obtained from Eq. (2). In order to keep continuity of the reconstructed image, a boundary overlap strategy is applied. Every two adjacent low-resolution cubes contain a one-voxel-wide overlap area. In the final reconstructed high-resolution image, every two high-resolution cubes have an s-voxel-wide overlap area (recall that s is the resolution magnification factor). In the overlapping part, voxel values are calculated by averaging the overlapped part from two cubes. Because the reconstruction work is based on floating numbers, a conventional segmentation operation is applied to recover discrete phases.

E. Postprocess

The input data of the LSSR method are discrete (segmented image), and the output data continuous ("tomographic" image) due to the chosen mathematical operations. In this step, we introduce the segmentation strategy used in this paper to transform the reconstructed "tomographic" image to a segmented image. In the case of Fontainebleau sandstone, which contains two phases, void and solid, a threshold is applied to divide the tomographic image into void and solid. This threshold is determined according to the porosity of the high-resolution training image to ensure that the segmented image has identical total porosity compared to the training image. Indiana limestone has three phases, macro-pore, solid, and porous matrix, which makes its segmentation more complex than that of Fontainebleau sandstone. The segmentation of the reconstructed Indiana limestone image is carried out as follows: First, the reconstructed image is segmented into two phases, solid and permeable phase (including macropore and porous matrix) according to the fraction of solid of the training image [see Fig. 6(a)]. Second, initial segmentation is undertaken within the permeable phase obtained from the first step to distinguish the macropore and porous matrix using a threshold which makes the fraction of macropores of the segmented image 30% less than that of the training image. For example, the fraction of macropores in the training image of Indiana limestone is f, then the threshold of intensity T satisfies that the fraction of macropores of the segmented image is $0.7 \times f$ [see Fig. 6(c)]. This is because the reconstructed image is not sharp enough to describe the boundary between solid and macropore just according to intensity [see Fig. 6(d)]. Third, intensity gradients are used as constraints to distinguish porous matrix and solid. In segmentation, high gradients imply direct contact between macroporous voxels (low intensity) and solid (high intensity) [see Fig. 6(e)]. So the high-gradient voxels are segmented as a macropore phase, which partially complements the absent part of macropore in step 2 [see Fig. 6(f)]. The fraction of macropore and porous matrix may be slightly different from the training image,

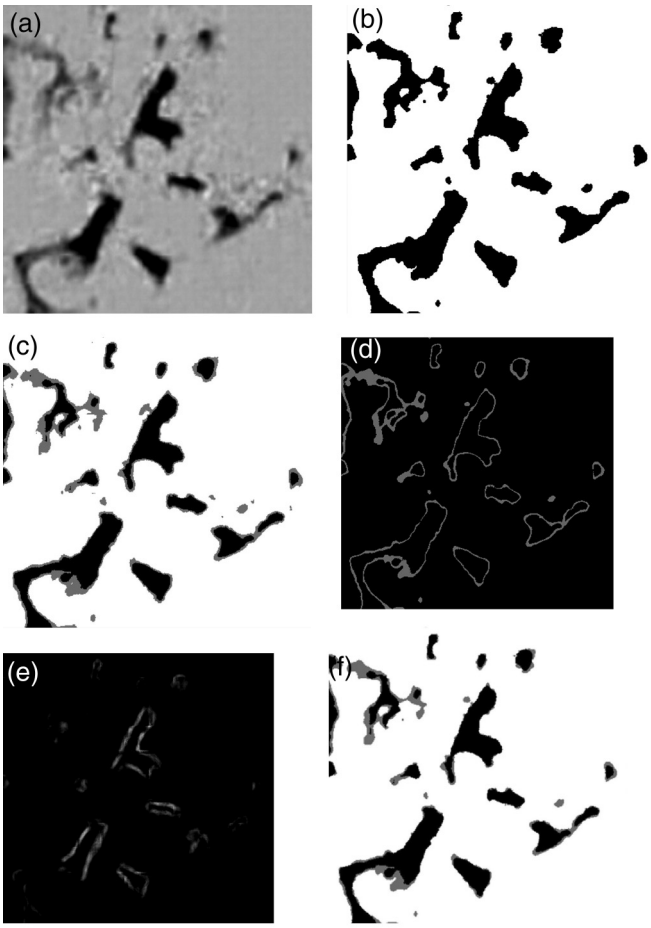

FIG. 6. Segmentation of the reconstructed "tomographic" image of Indiana limestone. (a) Reconstructed "tomographic" image; (b) segmented image with two phases, white:solid and black:pore space containing macropores and porous matrix; (c) this permeable phase in (b) is further segmented to macropore and porous matrix where the fraction of macropore is 15% less than that of the training image and black is macropore, white is solid, and gray is porous matrix; (d) porous matrix extracted from (c); (e) high-gradient voxels calculated based on image (a); (f) final segmented image obtained from (c), where the high-gradient porous matrix voxels are replaced in the macropore phase.

but the sum of their fractions is identical with the training image.

IV. MORPHOLOGICAL AND TRANSPORT PROPERTIES

To evaluate the relative performance of our reconstruction algorithm against popular methods we compare morphological measurements and transport properties on the actual high-resolution images with reconstructions derived by MPS and our proposed LSSR method. In the following we recapture a few pertinent morphological measures which are known to be sensitive discriminators of morphology as well as the chosen method to solve the Laplace equation for electrical conductivity.

A. Local porosity theory

Local porosity theory (LPT) is frequently used to characterize the porosity and connectivity fluctuation at different length scales in 3D digitized models [43,57]. Here we briefly introduce the basic definitions of the quantities of LPT.

1. Local porosity distribution

A measurement cell, $\mathbb{K}(r, L)$ denotes a cube centered at the lattice location r with side length of L. Within the cubic measurement cell $\mathbb{K}(r, L)$, the local porosity, $\phi(r, L)$ is defined as

$$\phi(r, L) = \frac{V(\mathbb{P} \cap \mathbb{K}(r, L))}{V(\mathbb{K}(r, L))}, \tag{10}$$

where $V(\mathbb{K}(r, L))$ denotes the volume of cell $\mathbb{K} \in \mathbb{R}^3$, and $V(\mathbb{P} \cap \mathbb{K}(r, L))$ is the pore space of $\mathbb{K}(r, L)$. The local porosity distribution $\mu(\phi, L)$ is given by

$$\mu(\phi, L) = \frac{1}{N} \sum_r \delta(\phi - \phi(r, L)), \tag{11}$$

where N denotes the number of cells and $\delta(\phi - \phi(r, L))$ is the Dirac delta function.

2. Local percolation probabilities

Local percolation probabilities characterize the connectivity of the pore space which controls the transport and propagation in porous media. The connectivity function is defined as

$$\Lambda_c(r, L) = \begin{cases} 1 & \text{if there is a path through} \\ & \mathbb{K}(r, L) \text{ in the } c \text{ direction,} \\ 0 & \text{otherwise.} \end{cases} \tag{12}$$

Here c denotes the direction of measurement, e.g., the x, y, and z directions, and $c = 3$ denotes all directions, whereas $c = \alpha$ denotes the x, y, or z direction. So $\Lambda_3 = 1$ indicates percolation in all directions, while $\Lambda_\alpha = 1$ indicates percolation in the x, y, or z direction. Then local percolation probabilities $\lambda_c(\phi, L)$ are given by

$$\lambda_c(\phi, L) = \frac{\sum_r \Lambda_c(r, L)\delta_{\phi\phi}(r, L)}{\sum_r \delta_{\phi,\phi(r,L)}}, \tag{13}$$

$$\delta_{\phi,\phi(r,L)} = \begin{cases} 1 & \text{if } \phi = \phi(r, L), \\ 0 & \text{otherwise,} \end{cases} \tag{14}$$

where $\delta_{\phi\phi(r,L)}$ is the Kronecker delta. Parameter $\lambda_c(\phi, L)$ describes the fraction of analyzed cells with L side length and porosity ϕ that are percolating in the c direction.

3. Total fraction of percolating cells

The total fraction of percolating cells $P_c(L)$ describes the percolation probability of measurement cells with side length of L in c direction. It is given by

$$P_c(L) = \int_0^1 \mu(\phi, L)\lambda_c(\phi, L)\, d\phi, \tag{15}$$

where $\mu(\phi, L)$ and $\lambda_c(\phi, L)$ are obtained from Eqs. (11) and (13), respectively.

B. Minkowski functionals

The Minkowski functionals are used as basic integral geometric measures to quantify the porous structure and are known to be sensitive descriptors of morphology [46–48]. After segmentation, the images to be analyzed are segmented into multiple phases. Integral geometry provides a complete set of $d+1$ additive Minkowski functionals for each phase, where d is the dimension of embedding space. For ambiguous configurations on the cubic lattice we use the 8- and 26-neighborhoods for mean and total curvature, respectively, and report the Minkowski functionals normalized to the volume of the considered domain V_t. The first functional M_0 is simply the total fraction of the target phase, which is given by

$$m_{0X} = M_0(X)/V_\mathrm{t} = V(X)/V_\mathrm{t}, \tag{16}$$

where $X \subset \Omega$ (Ω is the embedding space) is the space occupied by the target phase (e.g., the pore space in binary image). The other Minkowski functionals are defined through integrals over the surface of the pores denoted as δX, which unambiguously defines its shape or morphology of the pore structure at the given resolution. It can be described by

$$m_{1X} = M_1(X)/V_\mathrm{t} = \frac{1}{6}\int_{\delta X} ds/V_\mathrm{t}, \tag{17}$$

where ds is a surface element. The second integral measures the mean curvature of the interface

$$m_{2X} = M_2(X)/V_\mathrm{t} = \frac{1}{3\pi}\int_{\delta X}\left(\frac{1}{r_1}+\frac{1}{r_2}\right)ds/V_\mathrm{t}, \tag{18}$$

where r_1 and r_2 are the minimum and maximum radius of curvature for the surface element ds. This radius is positive for convex curvatures and negative for concave curvatures. The third integral measures the total curvature

$$m_{3X} = M_3(X)/V_\mathrm{t} = \int_{\delta X}\left(\frac{1}{r_1 r_2}\right)ds/V_\mathrm{t}, \tag{19}$$

which is related to the connectivity of the considered phase. For well-connected phases and a few isolated components this measure is typically negative and crosses zero to become positive close to the percolation threshold of the material [58].

C. Electrical conductivity

We solve the Laplace equation with charge conservation boundary conditions using a finite element method directly on the voxelized microstructure [59–61]. A potential gradient is applied in each coordinate direction and the system relaxed using a conjugate gradient technique to evaluate the field. We assign to the matrix of Fontainebleau (quartz) the conductivity $\sigma_m = 0$. For Indiana limestone we assign to the solid phase (calcite) a mineral conductivity of $\sigma_m = 0$, and to the intermediate a somewhat arbitrary conductivity of $\sigma_{im} = 0.0144\sigma_{fl}$. The latter was derived using an average background porosity suitable for the given image resolution resulting in a match to total porosity and applying Archie's law with $m = 2$ to convert this porosity into a conductivity (we do not claim that this is representative for the intermediate phase at the given resolution, but it is a good guess sufficient as a test for the quality of the reconstructions). In both cases we assign the fluid-filled pore phase a normalized conductivity $\sigma_{fl} = 1$. The principal components of the effective conductivity tensor σ_{ii} with subscripts $ii = xx, yy, zz$ are reported in the next section.

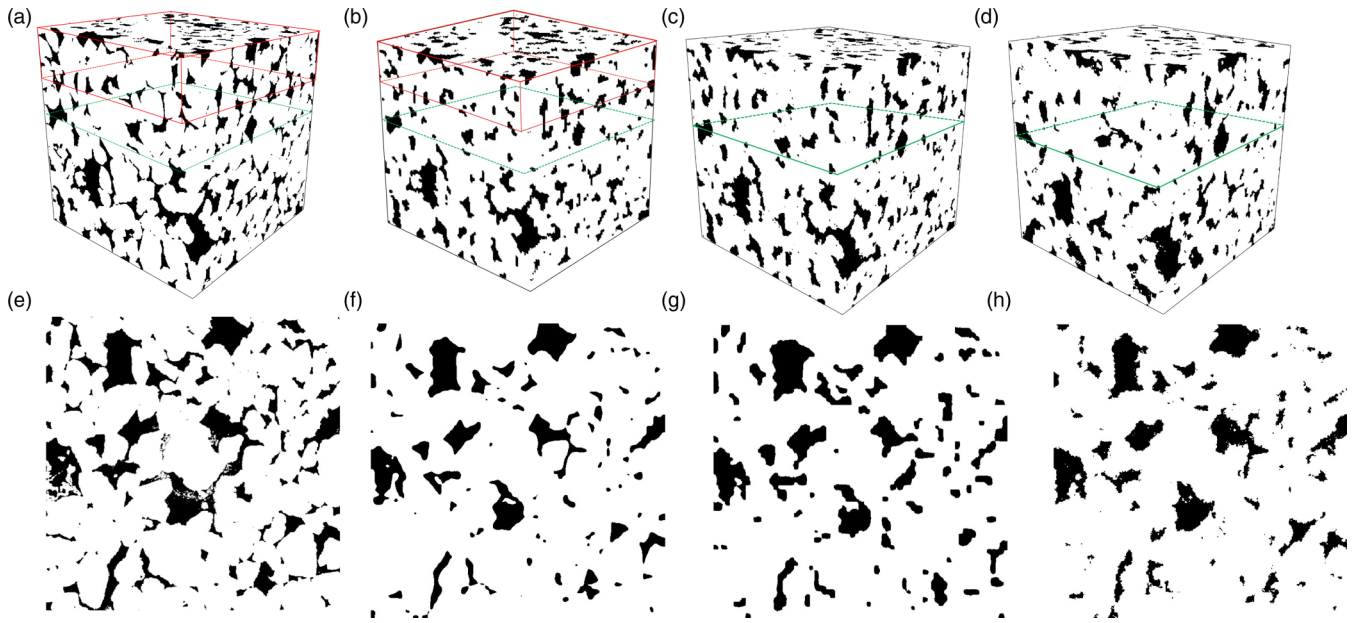

FIG. 7. Microstructure of Fontainebleau sandstone obtained from high- and low- resolution micro-CT image and reconstructed images through LSSR and MPS methods. Black is pore, and white is solid. (a) High-resolution image (600^3 voxel, $\epsilon = 2.9\,\mu$m). The red box labels the subset used as the high-resolution training image ($600 \times 600 \times 200$), and the green box represents the location of the slice presented in (e); (b) low-resolution image (75^3 voxel, $\epsilon = 23.2\,\mu$m). The red box labels the subset used as the low-resolution training image ($75 \times 75 \times 25$), and the green box indicates the location of the slice presented in (f); (c), (d) reconstructed high-resolution image by LSSR and MPS, respectively (600^3, $\epsilon = 2.9\,\mu$m). The green box in (c) and (d) represents the location of the slice presented in (g) and (h).

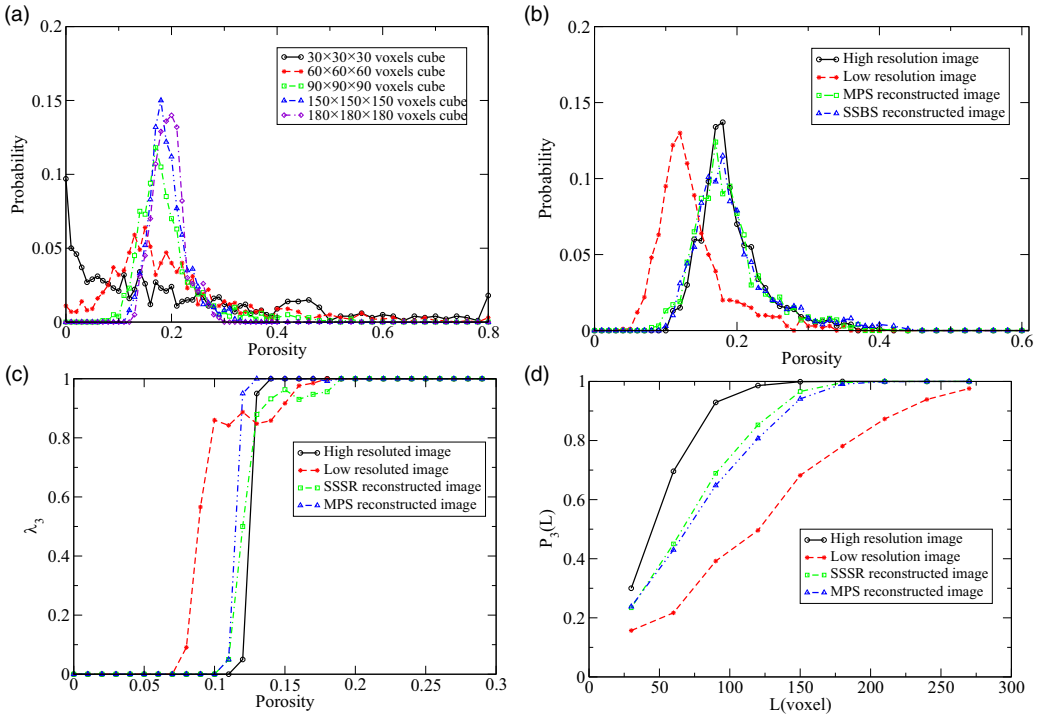

FIG. 8. (a) Local porosity distribution of the high-resolution image of Fontainebleau sandstone for different cube sizes; (b) local porosity distribution curve of high- and low-resolution images, LSSR and MPS reconstructed image, cube size 180^3 voxel; (c) local percolation probabilities (λ_3 is percolation probabilities in all XYZ directions) of high- and low-resolution images, LSSR and MPS reconstructed image; (d) total fraction of percolation cells [$P_3(L)$ indicates the percolation in both XYZ directions] of high- and low-resolution images, LSSR and MPS reconstructed image.

V. RESULTS

A. Image reconstruction: Fontainebleau sandstone

As detailed above, the Fontainebleau sandstone sample was acquired by micro-CT imaging with a resolution of $\epsilon = 2.9\,\mu$m (600 voxels length in the XYZ direction). This high-resolution image is reduced to a low-resolution image of $\epsilon = 23.2\,\mu$m (75 voxels length in the XYZ direction). As Fig. 7 shows, a $75 \times 75 \times 25$ subset is extracted from the low-resolution image as low-resolution training image. Its corresponding high-resolution part ($600 \times 600 \times 200$ voxel) is extracted from the high-resolution image as high-resolution training image. LSSR and MPS methods are applied to reconstruct higher-resolution images based on the entire low-resolution image.

LPT is used to quantify the performance of LSSR and MPS reconstruction techniques. The low-resolution image is interpolated to 600^3 voxel via nearest-neighbor interpolation. Thus, the voxel size of the four candidate images is identical. The panels in Fig. 8 show local porosity distribution curve, local percolation probabilities curve, total fraction of the percolation cells curve computed from high-resolution image, low-resolution image, LSSR reconstructed image, and MPS reconstructed image, respectively. Figure 8(a) illustrates the local porosity distribution of the high-resolution image with different cube size. From 30^3 voxels to 180^3 voxels size the distributions from the local porosity stabilize, and the minimum stable size is about 150^3 voxels. Thus, we use 180^3 voxels to compare the local porosity parameters of high- and low- resolution images and LSSR and MPS reconstructed images. From Fig. 8(b), it is clear that both LSSR and MPS reconstructed images improve the pore size distribution greatly. The local porosity distribution curves of the LSSR and MPS reconstructed image are close to each other with little difference. This closeness is also observed for the local percolation probabilities distribution shown in Fig. 8(c). From the total fraction of the percolation cells curve presented in Fig. 8(d), LSSR performs slightly better than the MPS reconstruction.

Table I illustrates the Minkowski functionals of high-resolution, low-resolution, LSSR reconstructed, and MPS reconstructed images of Fontainebleau sandstone. LSSR improves all Minkowski functionals of Fontainebleau sandstone and exhibits a better performance than MPS in terms of volume fraction (m_{0X}), surface density (m_{1X}), and total curvature (m_{3X}). Generally speaking, the performance of LSSR exceeds that of the MPS method for Fontainebleau. The limitation of

TABLE I. Normalized Minkowski functionals of Fontainebleau sandstone with respect to the pore space "p." HR, LSSR, MPS, and LR represent the high-resolution image, LSSR reconstructed image, MPS reconstructed image, and low-resolution image, respectively.

Method	HR	LSSR	MPS	LR
m_{0p}	0.1930	0.1899	0.1481	0.1353
m_{1p} (μm^{-1})	0.0251	0.0162	0.0157	0.0133
m_{2p} (μm^{-2})	3.47E-04	2.08E-04	2.52E-04	2.15E-04
m_{3p} (μm^{-3})	−7.13E-08	−6.00E-08	−1.80E-07	−3.99E-08

TABLE II. Principal components of the normalized effective conductivity of Fontainebleau sandstone calculated on the full 600^3 voxels domain. HR, LSSR, MPS, and LR represent the high-resolution image, LSSR reconstructed image, MPS reconstructed image, and low-resolution image, respectively.

Method	HR	LSSR	MPS	LR
σ_{xx}	0.0524	0.0227	0.0128	0.0125
σ_{yy}	0.0465	0.0232	0.0117	0.0121
σ_{zz}	0.0509	0.0242	0.0120	0.0129

the MPS method presented in this comparison may be due to the dependency of the statistical correlation functions for MPS on the training image. In other words, the output of the MPS method just reproduces the structural features of the training image rather than the expected entire sample.

Table II shows the results of the effective conductivity calculations for the three principal directions using the full 600^3 voxels domain. In all cases the conductivity calculated for the LSSR reconstruction is closest to the high-resolution original sample. This is consistent with the observations of better representation of percolation properties and total curvature as compared to MPS.

B. Image reconstruction: Indiana limestone

Consider now the 400^3 subset of the Indiana limestone sample described previously, scanned at a resolution of $\epsilon = 4.05\,\mu$m. Figure 9 depicts this subset, the corresponding low-resolution image of 100^3 voxel ($\epsilon = 16.2\,\mu$m), and the parts of the sample selected to extract high-resolution cubes and build up the training dictionaries. The size of the training domain is $100 \times 100 \times 20$ voxel in the low-resolution image, and $400 \times 400 \times 80$ voxel in the high-resolution image as indicated in Fig. 9, which further shows the reconstructed images derived using LSSR and MPS. We stress that we do not claim to select a representative subsample for Indiana limestone in the general sense, as it is difficult to define a representative elementary volume (REV) for this limestone, but rather work with a convenient subsample to illustrate the method.

Figure 10 illustrates measures to quantify the performance of the LSSR and MPS reconstructions: the local porosity distribution, local percolation probabilities, and total fraction of the percolation cells. Figure 10(a) presents the local porosity distribution of a high-resolution image with different cube size. With increasing domain size the distribution curve of local porosity is approaching a Gaussian distribution with a decreasing variance. In the following we use a 330^3 voxel domain to compare the local porosity parameters of high- and low-resolution images, and LSSR and MPS reconstructed images as a compromise between a reasonable size and narrow distribution of porosity. The local porosity distribution curves of high-and low-resolution image and LSSR and MPS reconstructed image are close to each other [see Fig. 10(b)]. In Fig. 10(c) although both LSSR and MPS improve the percolation ability compared to the low-resolution image, the performance of LSSR is better than the MPS method. Comparing the total fraction of the percolation cells for LSSR and MPS in Fig. 10(d), LSSR is close to MPS for small subsets (excluding extremely small) but is performing better for larger domains.

The reason why the features about local porosity distribution shown in Fig. 10(b) are similar, but totally different in terms of local percolation probabilities [see Fig. 10(c)] and total fraction of the percolation cells [see Fig. 10(d)], is because

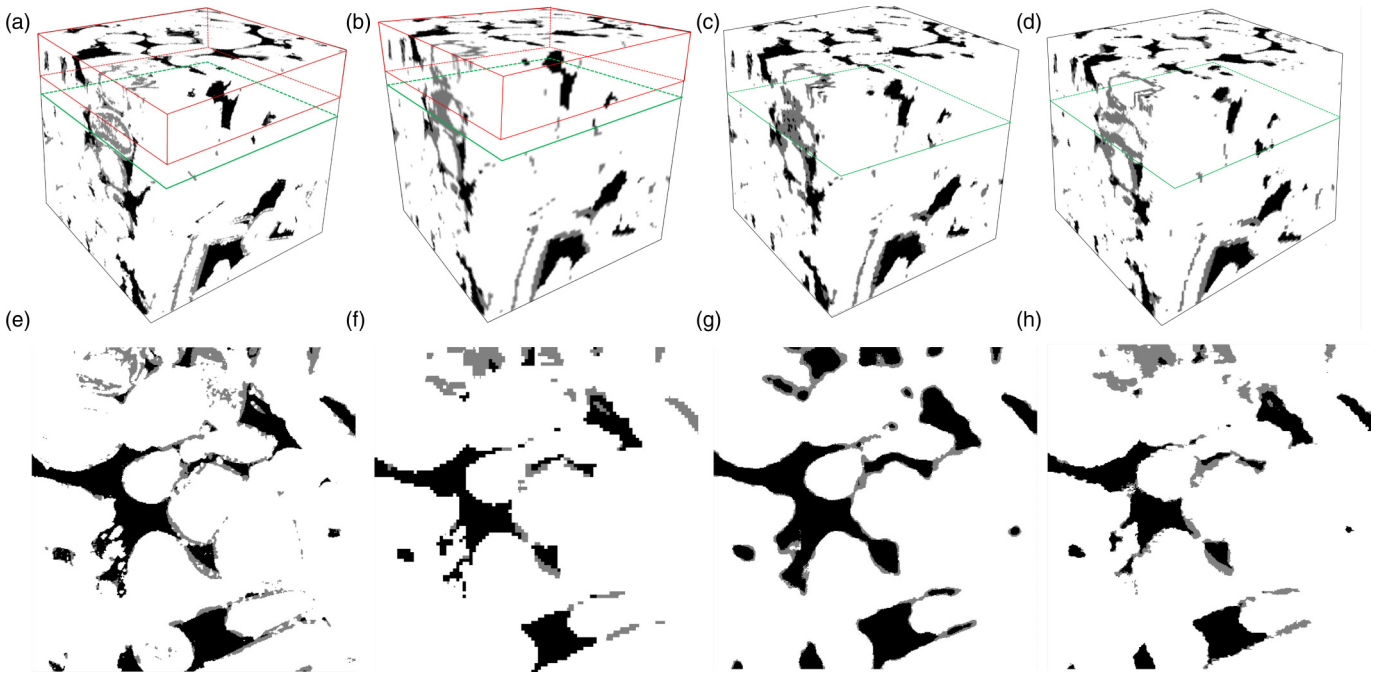

FIG. 9. Subsample cubes of Indiana limestone for (a) the high-resolution image (400^3 at $\epsilon = 4.05\,\mu$m), (b) the corresponding low-resolution cube (100^3 at $\epsilon = 16.2\,\mu$m), (c) the LSSR reconstruction, and (d) the MPS reconstruction. Black is macropore, gray is porous matrix, and white is solid. The red box indicates the training image subdomain of $400 \times 400 \times 80$ voxel (high resolution) and $100 \times 100 \times 20$ voxel (low resolution). The green frames indicate the location of the slice views given in panels (e)–(h).

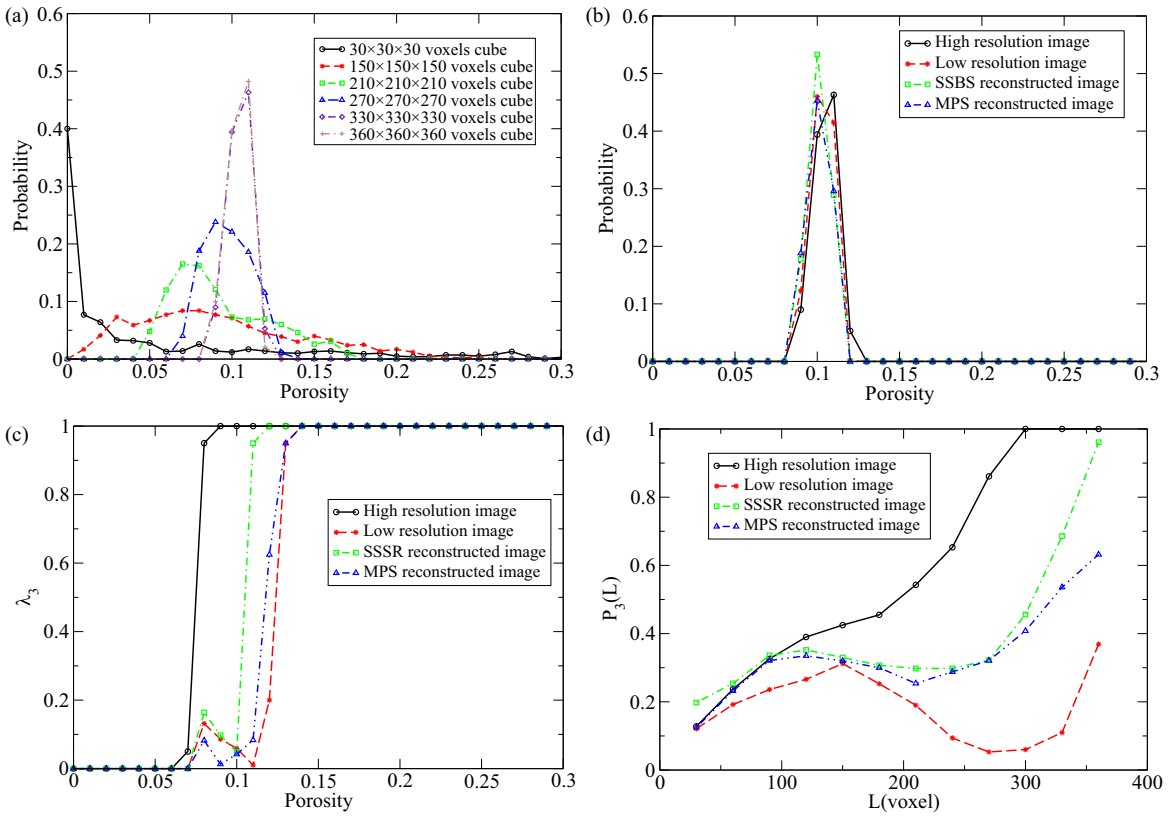

FIG. 10. (a) Local porosity distribution of the Indiana limestone high-resolution image for different cube sizes; (b) local porosity distribution curve of high- and low-resolution images, LSSR and MPS reconstructed image, and cube size is $330 \times 330 \times 330$ voxel^3; (c) the local percolation probabilities (λ_3 is percolation probabilities in all XYZ directions) of high- and low-resolution images, LSSR and MPS reconstructed image; (d) total fraction of the percolation cells [$P_3(L)$ indicates the percolation in all XYZ directions] of high- and low-resolution images, LSSR and MPS reconstructed image.

of the effect of the porous matrix. High- and low- resolution micro-CT images are segmented into three phases: macropore, porous matrix, and solid. Because macropores are large enough and Indiana limestone essentially has a bimodal pore size distribution, both low- and high-resolution micro-CT images capture the macroporosity with a reasonable accuracy. However, the number of intermediate-intensity microporous voxels is different, the latter of which are considered to have excellent percolation properties.

Table III illustrates the Minkowski functionals of high-resolution, low-resolution, and LSSR reconstructed and MPS reconstructed images of Indiana limestone. Different from Fontainebleau sandstone, Indiana limestone contains three phases (at voxel scale), and the Minkowski functionals of every phase are calculated separately. The proposed LSSR method still presents robust performance in this case with LSSR and MPS performing variably for m_2 and m_3, while LSSR leads in m_0 and m_1. Both reconstruction methods improve on the low-resolution direct comparison. Interestingly, the match in the Euler characteristic is generally better for MPS, while at the same time the percolation behavior (see Fig. 10) is matched better by LSSR.

We report in Table IV the effective conductivities calculated on the full 400^3 domains. For all directions the effective conductivity of the LSSR reconstruction is closest to the HR original image in terms of relative deviation.

C. Discussion

Comparing the performance of LSSR and MPS for the two different samples, we note that for the two-phase Fontainebleau sandstone LSSR was the superior method in almost all measures. For Indiana limestone, here utilized

TABLE III. Minkowski functionals of Indiana limestone. HR, LSSR, MPS, and LR represent the high-resolution image, LSSR reconstructed image, MPS reconstructed image, and low-resolution image, respectively. The reference phases are denoted as "p" (pore space), "i" (intermediate intensity porous matrix), and "s" (solid).

Method	HR	LSSR	MPS	LR
m_{0p}	0.0707	0.1021	0.0542	0.0479
m_{0i}	0.0389	0.0299	0.0356	0.0365
m_{0s}	0.8895	0.8680	0.9103	0.9156
m_{1p} (μm^{-1})	0.0075	0.0062	0.0047	0.0034
m_{1i} (μm^{-1})	0.0119	0.0099	0.0076	0.0041
m_{1s} (μm^{-1})	0.0134	0.0079	0.0079	0.0063
m_{2p} (μm^{-2})	2.84E-05	5.24E-05	5.45E-05	3.04E-05
m_{2i} (μm^{-2})	4.50E-04	2.66E-04	2.86E-04	1.12E-04
m_{2s} (μm^{-2})	−2.00E-04	−5.99E-05	−1.05E-04	−7.63E-05
m_{3p} (μm^{-3})	1.36E-06	−1.29E-08	5.61E-08	−1.68E-08
m_{3i} (μm^{-3})	−1.66E-06	−6.45E-07	−1.38E-06	−5.91E-07
m_{3s} (μm^{-3})	1.16E-07	−1.09E-08	−2.16E-08	−4.00E-08

TABLE IV. Principal components of the normalized effective conductivity of Indiana limestone calculated on the full 400^3 voxels domain. HR, LSSR, MPS, and LR represent the high-resolution image, LSSR reconstructed image, MPS reconstructed image, and low-resolution image, respectively.

Method	HR	LSSR	MPS	LR
$10^3\sigma_{xx}$	6.21	10.2	1.28	3.18
$10^3\sigma_{yy}$	4.79	8.11	1.79	3.08
$10^3\sigma_{zz}$	0.933	0.28	0.077	0.022

as a three-phase structure, all measures from local porosity theory considered are in favor of LSSR. However, for the Minkowski functionals the result was not as clear, with the curvature measures m_2 and m_3 slightly in favor of MPS with m_0 and m_1 in favor of LSSR. For both samples the effective conductivities are best matched by the LSSR reconstruction technique. We emphasize that for the introduction of the approach here we did not consider Indiana limestone as an n-phase material, e.g., where the intermediate phase consists of voxels of different porosity. Thus, the intermediate phase is homogenized here. A realistic calculation of conductivity would require both a larger sample (REV) and potentially a more detailed representation of small-scale heterogeneity. This is out of the scope of this work.

Practically, the application of LSSR is not affected by the number of phases, which poses important constraints on the MPS method. One basic limitation of MPS is that sufficient replicas have to be searched from the training image; otherwise the template size has to be decreased to reduce the difficulty of patterns matching. For increasing numbers of phases the difficulty of searching sufficient replicas increases rapidly. A smaller template has to be chosen, resulting in a reconstruction of reduced quality. In contrast, LSSR is based on a "decomposition-reconstruction," strategy and once the dictionary is trained, every low-resolution cube will be sparsely represented. The reconstruction is based on its sparse coefficients and the high-resolution dictionary. While the accuracy of LSSR also depends on the quality of the dictionary trained, a large increase of runtime with increasing phase number as in MPS can be avoided.

D. Time requirement

Because of the use of a "decomposition-reconstruction" strategy, the running speed of LSSR is much faster than MPS. As Table V shows, the time requirement of the MPS method depends on the training image size, template size, multigrid levels, phase numbers, and size of target low-resolution image. Larger training image size and template size will generate better results but slow down computations. Increasing grid levels and phase numbers will also increase the computation time significantly. The most time-consuming part of the MPS method is searching for matched patterns from the training image. In the LSSR method, this process is replaced by decomposition based on a previously trained dictionary, which is hundreds of times faster than traversing the training image for matching patterns. The most time-consuming part of the LSSR technique is training the low-resolution dictionary, which accounts for more than 90% of the image reconstruction (see Table V). However, once the dictionary is determined, it can be used for reconstruction of the whole image; here we have not done so due to computing resources in particular for MPS but will report on applications in the context of experimental measurements in the future. This makes the method reasonably scalable. It is not necessary to train the dictionary every time for different subsets within one sample.

TABLE V. Computation time of LSSR and MPS with different parameters. t_t: time, t_d: dictionary training time, t_r: reconstruction time, N_{PH}: number of phases, Mag.: magnification. Other parameters are sparsity threshold, 15; dictionary update loop number, 40; energy threshold for PCA, 90%; atom number of dictionary, 3000; number of training cube pairs, 30 000.

Method	Template	Domain	N_{PH}	Mag.	t_t (h)	t_d (h)	t_r (h)
MPS	7×7	600^3	2	$\times8$	7		
MPS	7×7	600^3	3	$\times4$	5.32		
LSSR	$4\times4\times4$	400^3	2	$\times4$	0.46	0.33	0.06
LSSR	$4\times4\times4$	400^3	3	$\times4$	0.46	0.33	0.06
LSSR	$3\times3\times3$	600^3	3	$\times8$	2.5	2.15	0.27
LSSR	$10\times10\times10$	400^3	3	$\times4$	14	12.6	0.35

VI. CONCLUSION

In this paper, we introduced a local-similarity-based statistic reconstruction method to improve the resolution of porous structure segmented from micro-CT images of rock samples. High-resolution and corresponding low-resolution subset pairs were extracted to analyze the porous structure relationship under different resolution. Their relationship is described by local similarity and represented by a compressed dictionary. The latter is then used to reconstruct a high-resolution image with low-resolution image constraints. The LSSR method applies a "Decomposition-Reconstruction" strategy instead of a "Search-Statistic" strategy, which is used in conventional reconstruction techniques. A sparse representation algorithm is used to realize this "Decomposition-Reconstruction" strategy for the porous structure reconstruction. We can make the following conclusions:

(1) The local-similarity phenomenon exists universally in the porous structure, which can be used to supervise the high-resolution porous structure reconstruction.

(2) The use of a "Decomposition-Reconstruction" strategy makes the LSSR method a computationally efficient method compared to conventional MPS.

(3) Because we apply a "Decomposition-Reconstruction" instead of a "Search-Statistic" strategy, the LSSR method can provide a more accurate porous structure than the MPS method, especially for multiple-phases reconstruction. This is due to two factors, the speed allowing a larger template size and the dictionary decomposition allowing description of patterns which have not been trained, since a set of coefficients can be found from the dictionary which transforms the low-resolution patch to a high-resolution one. This is different from MPS, where for each template a sufficient number of matched patterns must be found.

(4) A comparison between MPS and LSSR illustrates that LSSR is very competitive with MPS when comparing additive morphological measures, regional porosity, percolation statistics, and electrical conductivity.

ACKNOWLEDGMENTS

C.H.A. is the recipient of an Australian Research Council Australian Future Fellowship (FT120100216). This research was undertaken with the assistance of resources and services from the National Computational Infrastructure (NCI), which is supported by the Australian Government.

APPENDIX

Pseudocode of LSSR reconstruction algorithm

In order to describe the work flow of the LSSR reconstruction technique more clearly, we provide here a pseudocode of the LSSR algorithm. We divide the algorithm into an input data section and the required steps to generate the final output, the high-resolution reconstructed image of porous structure.

Input data

I	Low resolution target image
I_{high}	3D high-resolution training image
I_{low}	3D low-resolution training image
s	Magnification factor
c_l	Scanning window size for low-resolution image
c_h	Scanning window size for high-resolution image ($c_h = c_l s$)
L	Sparsity threshold
K	Dictionary update loop number
T	Energy threshold for PCA
N_d	Atom number of dictionary
N_p	Number of training cube pairs

Step 1

Extract N_p training image cube pairs from I_{high} and I_{low} with a window size of ${c_l}^3$ and ${c_h}^3$, respectively.

Step 2

Organize low-resolution cubes into a ${c_l}^3 \times N_p$ matrix, LR, and every column of LR is a low-resolution image cube.

Step 3

Organize high-resolution cubes into a ${c_h}^3 \times N_p$ matrix HR, where every column of HR represents a high-resolution image cube.

Step 4

Training low-resolution dictionary:

(1) Generate a ${c_l}^3 \times N_d$ matrix randomly as initial low-resolution dictionary, denoted by D_l

(2) Trainlow-resolution dictionary and sparse coefficient using K-SVD and OMP algorithm:

training: for $m = 1$ to K, do

(a) Initialize the sparse coefficient matrix, C, as $N_d \times N_p$ zero matrix

(b) Using OMP for sparse coding:

OMPsparse: for $n = 1$ to N_p, do

(i) Initialize the basis matrix $B_0 = \{\}$ and $l_{r0}^n = l_r^n$; (l_r^n is the nth column vector of LR)

(ii) Compute the inner conduction between l_{r0}^n with every atom of D_l and choose the closest atom, α_0 and record its column number p_0

(iii) Update the $B_1 = B_0 \cup \{\alpha_0\}$

(iv) Compute the coefficient of l_r^n, C_n under the basis matrix of B_1 by $C_n = {B_1}^{\dagger} l_r^n$ (${B_1}^{\dagger}$ is the pseudo-inverse of B_1)

(v) Compute the residual vector of l_{r0}^n, l_{r1}^n ($l_{r1}^n = l_{r0}^n - B_1 C_n$)

(vi) Compute the inner conduction between l_{r1}^n with every atom of D_l and choose the closest atom, α_1 and record its column number p_1

(vii) Update the $B_0 = B_1 \cup \{\alpha_1\}$ and $l_{r0}^n = l_{r1}^n$

(viii) Repeat steps ii to vii until the dimensionality of C_n is equal to L (sparsity threshold)

(ix) Put every element of C_n in to the nth column of C according to its corresponding column number p_0 to p_L

end *OMPsparse*

(c) K-SVD for updating dictionary:

dicUpdate: for $n = 1$ to N_d, do

(i) Find out the location of nonzero elements of nth row in sparse coefficient matrix C, and this location records which low-resolution image cube used the nth atom in dictionary

(ii) Extract the columns which used the nth atom and organize them as a ${c_l}^3 \times k$ matrix, LR_t (k is the number of qualified columns)

(iii) Extract the coefficient columns corresponding to LR_t and organize them as a $k \times N_d$ matrix, C_t

(iv) Compute the error matrix, E_n, by $E_n = LR_t - D_l C_t$

(v) Decompose E_n by SVD algorithm, $E_n = USV^T$

(iv) Use the first column of U(corresponding to the largest singular value) replace the nth atom in dictionary

end *dicUpdate*

end *training*

Step 5

Dimensionality reduction by PCA:

(1) Compute the autocovariance matrix of HR (mean-residual normalized), denoted by C_x ($ch^3 \times ch^3$ matrix)

(2) Decompose the C_x by SVD operation, $C_x = P\Sigma P^T$ [$\Sigma = \text{diag}(\sigma_1^2, \sigma_2^2, \sigma_3^2, \ldots, \sigma_{ch^3}^2)$ and $\sigma_1^2 \geqslant \sigma_2^2 \geqslant \sigma_3^2 \geqslant \cdots \geqslant \cdots \sigma_{ch^3}^2$]

(3) Choose the first m [m is determined by Eq. (3)] columns of P, denoted by K_t and K_t is the transform matrix for dimensionality reduction

(4) Dimensionality reduce of high-resolution training cubes, HR_r can be obtained by $HR_r = K_t HR$

Step 6

Compute the high-resolution dictionary D_h, $D_h = HRAC^{\dagger} = HRC^T CC^{T-1}$ (C is full rank in rows)

Step 7

Decomposition and reconstruction:

(1) Raster scan the target low-resolution image, I and divide it into small cubes with a size of $cl \times cl \times cl$ voxel^3, make sure every two adjacent cubes have one voxel width overlap areas

(2) Organize these low-resolution cubes into a $cl^3 \times N$ (N is the number of cubes) matrix, LR_t, and every column of LR_t is an low-resolution image cube

(3) Sparse coefficient matrix of LR_t, C_t can be obtained by step 4

(4) High-resolution cubes, HR_t, can be obtained by $HR_t = D_h \times C_t$

(5) Combine these high-resolution cubes together to get a high-resolution image, and the overlap part is averaged by adjacent cubes.

[1] Z. Hashin and S. Shtrikman, J. Mech. Phys. Solids **11**, 127 (1963).
[2] P. Sheng, Geophysics **56**, 1236 (1991).
[3] P. A. Berge, J. G. Berryman, and B. P. Bonner, Geophys. Res. Lett. **20**, 2619 (1993).
[4] G. W. Milton, Phys. Rev. Lett. **46**, 542 (1981).
[5] C. H. Arns, M. A. Knackstedt, and N. S. Martys, Phys. Rev. E **72**, 046304 (2005).
[6] I. Fatt *et al.*, Petrol. Trans. **207**, 144 (1956).
[7] J. A. Quiblier, J. Colloid Interface Sci. **98**, 84 (1984).
[8] C. L. Y. Yeong and S. Torquato, Phys. Rev. E **57**, 495 (1998).
[9] H. Okabe and M. J. Blunt, Phys. Rev. E **70**, 066135 (2004).
[10] P. Adler, C. Jacquin, and J. Quiblier, Int. J. Multiphase Flow **16**, 691 (1990).
[11] P. Adler and J.-F. Thovert, Appl. Mech. Rev. **51**, 537 (1998).
[12] M. Ioannidis and I. Chatzis, J. Colloid Interface Sci. **229**, 323 (2000).
[13] P. Levitz, Adv. Colloid Interface Sci. **76–77**, 71 (1998).
[14] A. P. Roberts and S. Torquato, Phys. Rev. E **59**, 4953 (1999).
[15] E. S. Kikkinides and V. N. Burganos, Phys. Rev. E **59**, 7185 (1999).
[16] E. S. Kikkinides and V. N. Burganos, Phys. Rev. E **62**, 6906 (2000).
[17] E. Kikkinides, K. Stoitsas, V. Zaspalis, and V. Burganos, J. Membr. Sci. **243**, 133 (2004).
[18] B. Biswal and R. Hilfer, Physica A **266**, 307 (1999).
[19] R. Hilfer, Phys. Rev. B **44**, 60 (1991).
[20] S. Torquato and B. Lu, Phys. Rev. E **47**, 2950 (1993).
[21] M. D. Rintoul and S. Torquato, J. Colloid Interface Sci. **186**, 467 (1997).
[22] C. L. Y. Yeong and S. Torquato, Phys. Rev. E **58**, 224 (1998).
[23] C. Manwart, S. Torquato, and R. Hilfer, Phys. Rev. E **62**, 893 (2000).
[24] M. Talukdar, O. Torsaeter, M. Ioannidis, and J. Howard, Transp. Porous Media **48**, 101 (2002).
[25] P. Čapek, V. Hejtmánek, L. Brabec, A. Zikánová, and M. Kočiřík, Transp. Porous Media **76**, 179 (2009).
[26] J.-F. Thovert, F. Yousefian, P. Spanne, C. G. Jacquin, and P. M. Adler, Phys. Rev. E **63**, 061307 (2001).
[27] C. H. Arns, M. A. Knackstedt, and K. R. Mecke, Phys. Rev. Lett. **91**, 215506 (2003).
[28] C. H. Arns, M. A. Knackstedt, and K. R. Mecke, Phys. Rev. E **80**, 051303 (2009).
[29] J.-F. Thovert and P. M. Adler, Phys. Rev. E **83**, 056116 (2011).
[30] S. Bryant and M. Blunt, Phys. Rev. A **46**, 2004 (1992).
[31] D. Coelho, J.-F. Thovert, and P. M. Adler, Phys. Rev. E **55**, 1959 (1997).
[32] J.-P. Latham, Y. Lu, and A. Munjiza, Géotechnique **51**, 871 (2001).
[33] P.-E. Øren and S. Bakke, Transp. Porous Media **46**, 311 (2002).
[34] M. Politis, E. Kikkinides, M. Kainourgiakis, and A. Stubos, Microporous Mesoporous Mater. **110**, 92 (2008).
[35] M. Kainourgiakis, E. Kikkinides, T. Steriotis, A. Stubos, K. Tzevelekos, and N. Kanellopoulos, J. Colloid Interface Sci. **231**, 158 (2000).
[36] K. Wu, M. I. Van Dijke, G. D. Couples, Z. Jiang, J. Ma, K. S. Sorbie, J. Crawford, I. Young, and X. Zhang, Transp. Porous Media **65**, 443 (2006).
[37] J. G. Berryman, J. Appl. Phys. **57**, 2374 (1984).
[38] S. Strebelle, K. Payrazyan, J. Caers *et al.*, in *SPE Annual Technical Conference and Exhibition*, SPE 77425 (Society of Petroleum Engineers, 2002), pp. 1–10.
[39] H. Okabe and M. J. Blunt, Water Resour. Res. **43**, W12S02 (2007).
[40] B. Biswal, P. E. Oren, R. J. Held, S. Bakke, and R. Hilfer, Phys. Rev. E **75**, 061303 (2007).
[41] S. V. Korneev, X. Yang, J. M. Zachara, T. D. Scheibe, and I. Battiato, Water Resour. Res. **54**, 2871 (2018).
[42] A. Comunian, P. Renard, and J. Straubhaar, Comput. Geosci. **40**, 49 (2012).
[43] R. Hilfer, Phys. Rev. B **45**, 7115 (1992).
[44] R. Hilfer, T. Rage, and B. Virgin, Physica A **241**, 105 (1997).
[45] K. R. Mecke, in *Statistical Physics and Spatial Statistics, The Art of Analyzing and Modeling Spatial Structures and Pattern Formation*, Lecture Notes in Physics Vol. 554, edited by K. R. Mecke and D. Stoyan (Springer, Berlin, 2000), pp. 111–184.
[46] C. H. Arns, M. A. Knackstedt, W. V. Pinczewski, and K. R. Mecke, Phys. Rev. E **63**, 031112 (2001).
[47] C. H. Arns, M. A. Knackstedt, W. V. Pinczewski, and K. R. Mecke, Colloids Surf. A **241**, 351 (2004).
[48] C. H. Arns, M. A. Knackstedt, and K. R. Mecke, J. Microscopy **240**, 181 (2010).
[49] H. Chang, D.-Y. Yeung, and Y. Xiong, in *Proceedings of the 2004 IEEE Computer Society Conference on Computer Vision and Pattern Recognition*, CVPR 2004, Vol. 1 (IEEE, 2004), pp. I275–I282.
[50] R. Zeyde, M. Elad, and M. Protter, Lect. Notes Comput. Sci. **6920**, 711 (2010).

[51] R. W. Hamming, Bell Syst. Tech. J. **29**, 147 (1950).
[52] G. Mariethoz, P. Renard, and J. Straubhaar, Water Resour. Res. **46**, W11536 (2010).
[53] A. P. Sheppard, R. M. Sok, and H. Averdunk, Physica A **339**, 145 (2004).
[54] I. Arganda-Carreras, V. Kaying, C. Rueden, K. W. Eliceiri, J. Schindelin, A. Cardona, and H. S. Seung, Bioinformatics **33**, 2424 (2017).
[55] W. Dong, L. Zhang, G. Shi, and X. Wu, IEEE Trans. Image Proc. **20**, 1838 (2011).
[56] M. Aharon, M. Elad, and A. Bruckstein, IEEE Trans. Signal Proc. **54**, 4311 (2006).
[57] F. Latief, B. Biswal, U. Fauzi, and R. Hilfer, Physica A **389**, 1607 (2010).
[58] K. R. Mecke and A. Seyfried, Europhys. Lett. **58**, 28 (2002).
[59] E. J. Garboczi and J. F. Douglas, Phys. Rev. E **53**, 6169 (1996).
[60] E. J. Garboczi, NIST Internal Report 6269 (1998), http://ciks.cbt.nist.gov/monograph.
[61] C. H. Arns, M. A. Knackstedt, W. V. Pinczewski, and W. B. Lindquist, Geophys. Res. Lett. **28**, 3361 (2001).